Society for Science and Education
United Kingdom

ISSN: 2055 - 1266
Volume 4 No 6
Dec 2017

Journal of Biomedical Engineering and Medical Imaging

TABLE OF CONTENTS

EDITORIAL ADVISORY BOARD

DISCLAIMER

All the contributions are published in good faith and intentions to promote and encourage research activities around the globe. The contributions are property of their respective authors/owners and the journal is not responsible for any content that hurts someone's views or feelings etc.

SOCIETY FOR SCIENCE AND EDUCATION UNITED KINGDOM

JBEMi JOURNAL OF BIOMEDICAL ENGINEERING AND MEDICAL IMAGING

ISSN: 2055-1266

Computational Analysis of Histological Images of Tissue Engineered Cartilage for Evaluation of Scaffold Cell Migration

[1]Thomas Lepiarz, [1]Ulla Wenzel, [1]Michael Munz, [2]Katja Hasch, [2]Eva Goldberg-Bockhorn, [2,3]Nicole Rotter, [1]Martin Hessling

[1]Institute of Medical Engineering and Mechatronics, Ulm University of Applied Sciences, Germany

[2]Department of Otorhinolaryngology, Ulm University Medical Center, Ulm, Germany

[3]Department of Otorhinolaryngology, Mannheim University Medical Center, Mannheim, Germany

lepiarz@mail.hs-ulm.de, wenzel@hs-ulm.de, michael.munz@hs-ulm.de, Katja.Hasch@uniklinik-ulm.de, eva.goldberg@uniklinik-ulm.de, Nicole.Rotter@uniklinik-ulm.de, hessling@hs-ulm.de

ABSTRACT

Human chondrocytes were seeded on porcine collagen scaffolds and cultivated for up to six weeks in a cartilage bioreactor. To evaluate the influence of cultivation parameters on the proliferation and migration of the cells into the scaffolds, microscopic images from histological and immunohistochemical stainings were taken and digitalized. For evaluation of these pictures, image processing algorithms have been developed that enable quantitative conclusions with regards to aggrecan and collagen type I concentrations as well as the number of cell nuclei within the scaffold and respective migration depths. Furthermore, the number of scaffold lacunae and their orientation relative to the scaffold´s surface can be determined. A total of 85 images of different cultivations under various conditions were processed and the results evaluated by an expert. Additionally, the findings were related to results of available conventional biochemical laboratory results. The outcomes showed very few minor flaws but were valid in most cases. Some findings - as the distribution of the total cell number between cells on the surface and inside the scaffold - are superior to conventional laboratory methods that do not give this insight. A further advantage compared to the established common expert evaluation of these images, is that this approach is faster and less dependent on the judgement of the individual expert and offers quantitative results. The software development will be continued and applied for further optimizing of cartilage culture conditions.

Keywords: image analysis; histological images; cartilage; scaffolds; bioreactor

1 Introduction

Structural and functional facial cartilage defects are mainly caused by congenital lesions, traumata and cancer. Multiple and complex surgical interventions are necessary to repair those defects [1]. Tissue

DOI: 10.14738/jbemi.46.3854
Publication Date: 3rd December 2017
URL: http://dx.doi.org/10.14738/jbemi. 46.3854

Engineering (TE) with autologous cells is an alternative therapeutical approach. Human chondrocytes are seeded on porous scaffolds and cultivated to form new vital cartilage. During ex vivo culture cells proliferate and migrate into the scaffold prior to implanting the construct into the patient. Unfortunately, cultivating chondrocytes on 3D scaffolds to form new vital cartilage is very challenging and success is not guaranteed due to the complex influencing factors, which are not fully understood yet. Next to biocompatibility, biodegradability, biochemical and mechanical properties the structure of the scaffold is a decisive factor. Open and porous scaffolds are essential for nutrition, proliferation and migration of cells as well as for the development of new cartilage tissue [2,3]. Decellularized porcine cartilage scaffolds seem to be a promising material to restore cartilage defects. The decellularization process eliminates all immunogenic components of the cartilage in particular cells and glycosaminoglycans (GAG) so that a pure chondroconductive collagen scaffold remains [4]. To assess the quality of cell growth and migration it is common to take microscopic images from ultrathin sections of the preparations after immunostaining of selected components. These images are usually interpreted by experts whose evaluation depends on their skills and training. Furthermore, even a highly competent professional has difficulties quantifying values like average migration depth, cell numbers and concentrations or average lacunae properties. This makes a precise and objective diagnosis based on histological images an ongoing challenge for scientists.

A computer-aided diagnosis with image processing algorithms and techniques could be an alternative approach for the evaluation of histochemical images [5,6] but has not been applied to chondrocyte migration into scaffolds so far. Among the advantages are the reproducibility of the results, the possibility of determining quantitative values for the comparison of images and the speed of an automated computer-based image evaluation.

Unfortunately, there are no standard procedures or standard algorithms for performing meaningful analyses. A relevant review about computational histological analysis of hematoxylin-eosin (H&E), fluorescence and multispectral images is presented by Fuchs and Buhmann in [7]. The authors discuss the preprocessing of images and segmentation of different tissue components to distinguish relevant from irrelevant information. Those regions of interest (ROI) are characterized by defined textures or distinct colors and shades. For additional image processing mathematical-morphological operations are utilized which were first mentioned by George Matheron in [8]. Morphological processing operations require the interaction of the given image pixel with an external set of pixels which form a structure element (SE). They are utilized to remove insignificant structures by retaining the characteristics of an image.

In this paper a novel approach of segmenting histological images is presented that should offer objective and quantitative data from histochemically prepared cartilage sample images for improving future cartilage cultivation parameters. Ultrathin sections from decellularized porcine septal cartilage scaffolds seeded with human nasal chondrocytes were analyzed. The results of 85 image analyses were controlled by an expert and compared to the results of standard laboratory methods.

2 Methods

2.1 Material and Histological Image Acquisition

3D scaffolds of decellularized porcine nasal septum cartilage were seeded with human nasal chondrocytes and then cultivated in a bioreactor (BR) with automated nutrient and gas supply for up to 6 weeks.

Samples were taken from culture after 14, 28 and 42 days [9,10]. Additionally, statical cultivations without medium flow were conducted for comparison to the BR. In total three cultivation attempts were evaluated. The immunohistochemical staining procedures for aggrecan and collagen type II are presented in [11], for collagen type I and histological alcian blue staining in [12]. All samples were analyzed with a Zeiss Observer.D1 Microscope and visual recordings were performed with the Zeiss AxioCam MRc Camera with 1380x1040 pixels. For this purpose, the Zeiss software package AxioVision was employed. The images were taken with a tenfold microscope magnification by a skilled medical technician. Typical sample images with many chondrocytes in a cell pellet on top of the scaffolds can be found in **Figure 1**. It is also perceptible that the more important composition within the scaffold may be very different from the situation in the cell pellet.

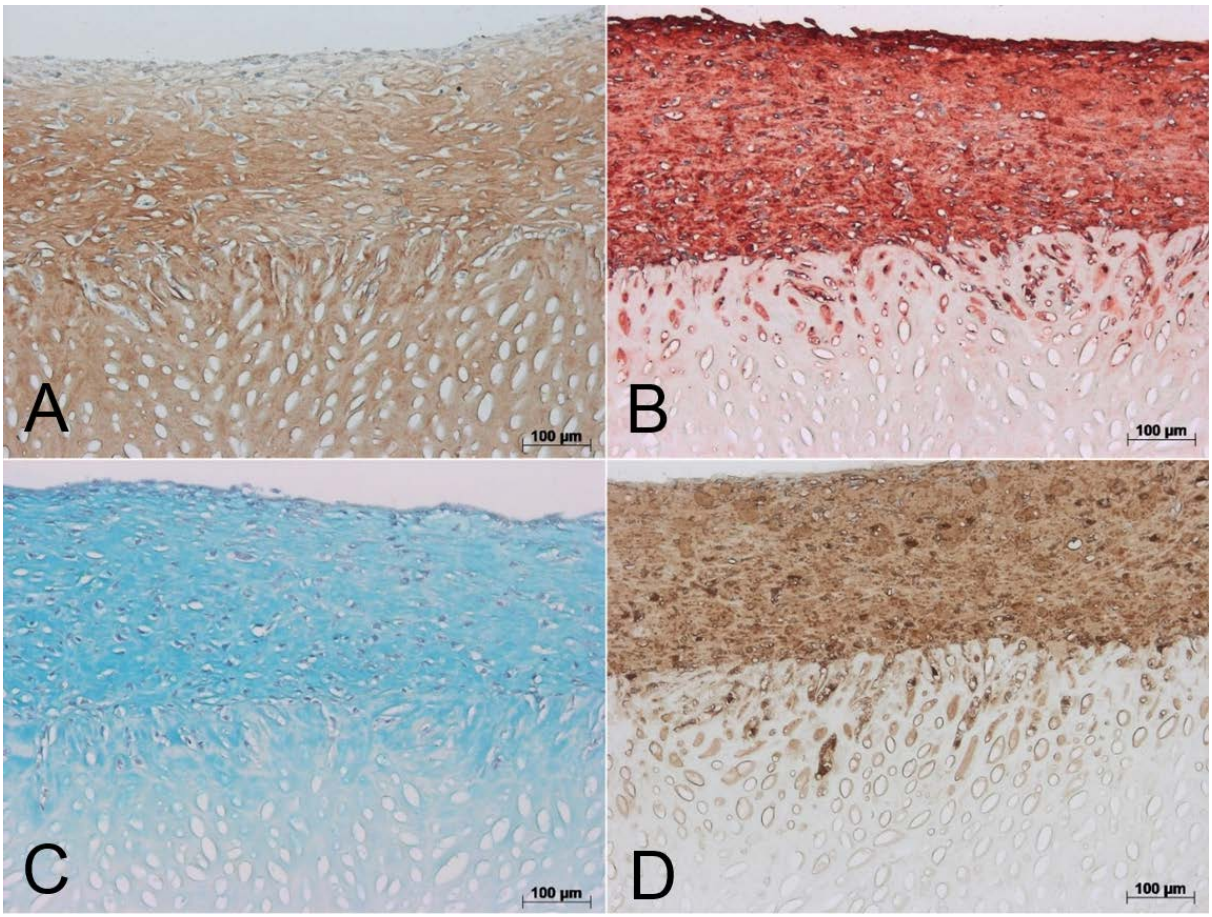

Figure 1: Examples of histological images of decellularized porcine cartilage scaffolds seeded with human chondrocytes. A: Immunohistochemical staining to detect collagen type II as component of the scaffold and synthesis product of the seeded cells (brown colouring). B: Tissue section after immunohistochemical staining of collagen type I, which is produced by the seeded cells (red-brown colouring). C: Alcian blue staining reveals the typical blue coloring of the muco-polysaccharids produced by the chondrocytes and the darker cell nuclei whereas the scaffold's matrix is nearly transparent. D: Brown colouring indicates aggrecan production of the cells.

2.2 Image Processing

The segmentation algorithm is divided into several stages and summarized in Figure 2. The algorithm was implemented and realized with the Image Processing Toolbox™ in MATLAB®, Version R2016b (The MathWorks, Inc.). For the observer's comprehension of every single process step a user interface was designed.

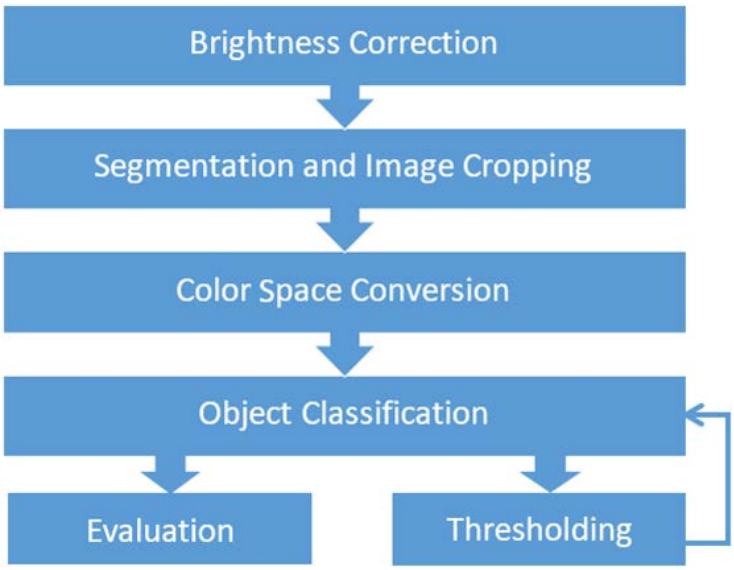

Figure 2: Summarized segmentation process.

2.3 Brightness Correction

Because of different illumination conditions during image acquisition and variations in the staining procedures the images differ in brightness and color intensities. To simplify the image analysis a first image processing step normalizes the images and reduces illumination and staining differences.

All pixels contain information about red, green and blue intensities. A region of interest (ROI) is manually selected, which complies with the background. This ROI with the size $w \times h$ is a subimage J of the original image G.

The average red, green and blue channel values of the image J are calculated:

$$R_{mean} = \frac{1}{wh}\sum_{j=1}^{h}\sum_{j=1}^{w} J(i,j,1), G_{mean} = \frac{1}{wh}\sum_{j=1}^{h}\sum_{j=1}^{w} J(i,j,2), B_{mean} = \frac{1}{wh}\sum_{j=1}^{h}\sum_{j=1}^{w} J(i,j,3)$$

A new image F with size $w \times h$ is created containing the averaged values R_{mean}, G_{mean} and B_{mean} in any pixel. By subtracting F from G, a new image I is calculated as depicted in Figure 3.

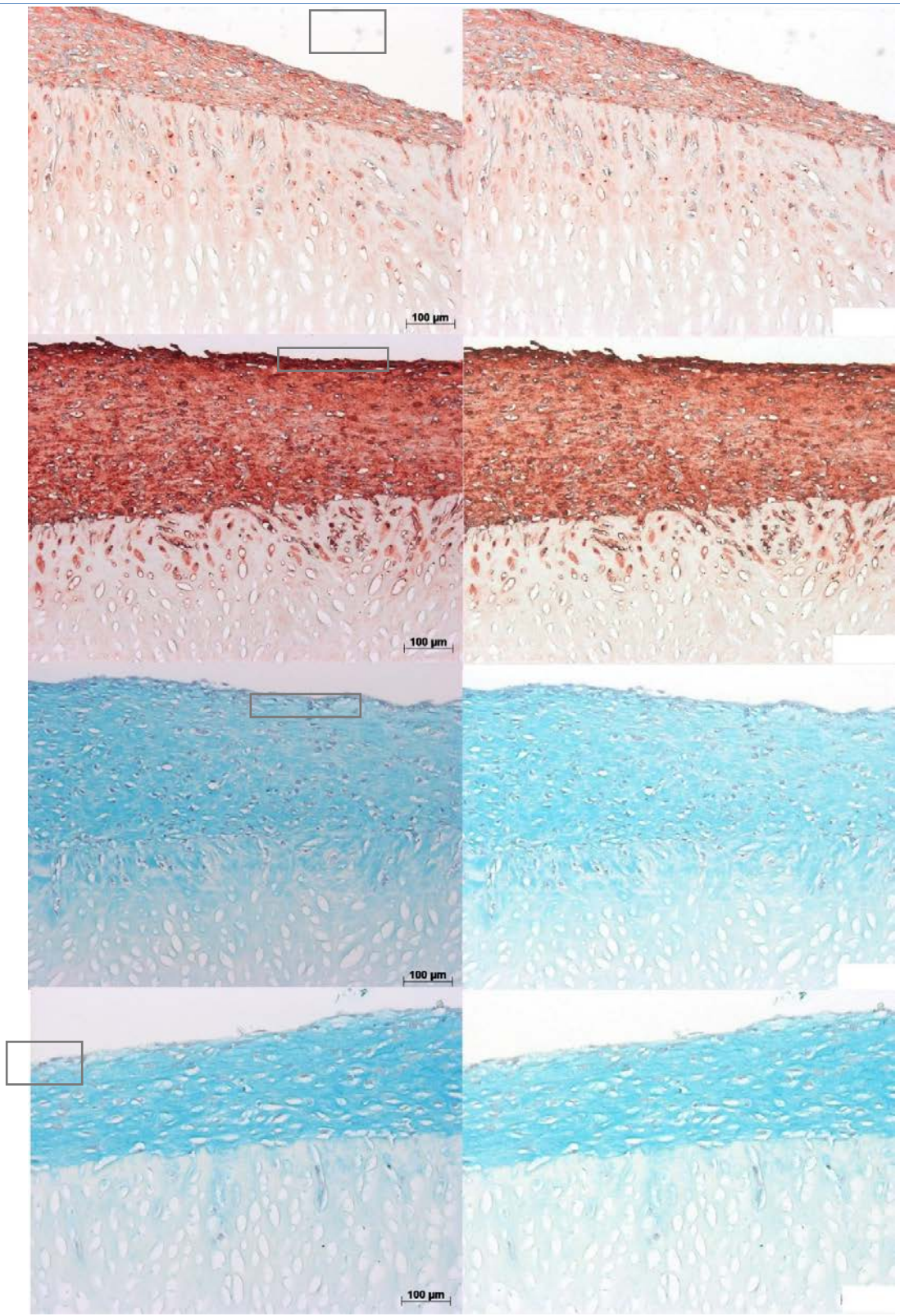

Figure 3: Four examples of brightness correction. In the two red images above collagen type I is stained. The images below depict alcian blue stained samples. For each kind of staining an example for a brighter and darker original image is given to prove that the normalized results are comparable. The green squares in the uncorrected pictures on the left side represent the area, which is averaged (right pictures). Scales in the lower right corner are removed because they interfere with the image analysis.

2.4 Segmentation and Image Cropping

The aim of image segmentation is to highlight or differentiate objects from each other or from the environment. Here, it is necessary to separate the cell pellet on the surface of the scaffold from the scaffold matrix, in which the cells should migrate and differentiate. Therefore, several edge points of a ROI are manually selected in the image on the surface line of the scaffold. These ROI points are used as a polygon separation line. A binary mask is created with white pixels above and black pixels below this polygon. The binary mask is then employed for separating the scaffold (SF) from the cell pellet (CP) on top of the scaffold which results in two images I(SF) and I(CP), as illustrated in Figure 4.

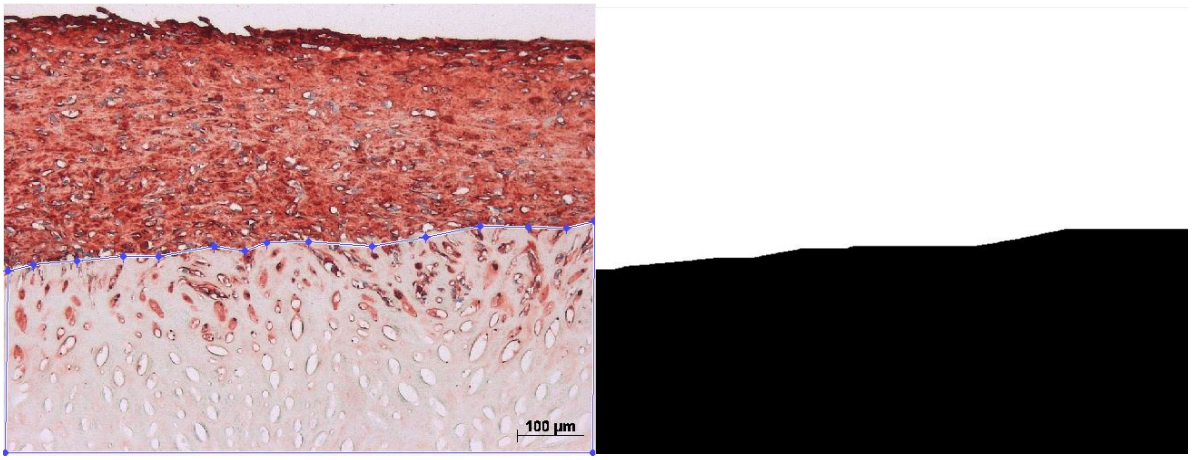

Figure 4: Blue dots and lines represent selected ROI (left) and the resulting binary image (right).

2.5 Color Space Conversion

For further segmentation, the images I(SF) and I(CP) are converted from RGB color space into the HSV color space. This transformation changes the pixel information from red, green and blue intensity into Hue (H), Saturation (S) and Value (V), which represents the color, the purity of a color and the luminous intensity of a pixel. H is defined in a range between 0 and 360 whereas S and V are defined in a range between 0 and 1. The HSV color space is illustrated in Figure 5 and further explained in [13].

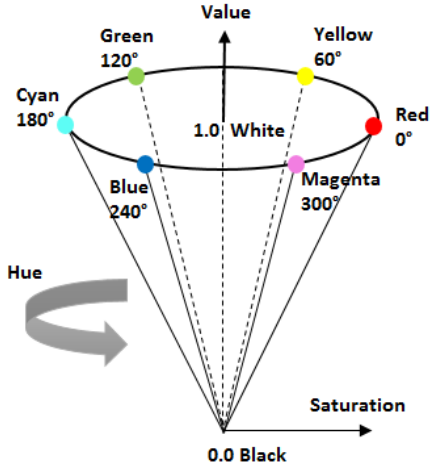

Figure 5: Illustration of HSV color space.

Active chondrocytes produce collagen type I & II, glycosaminoglycans and aggrecan, with ratios depending on their differentiation status. The concentrations of these substances can be evaluated after the immunohistochemical staining and image analysis. Due to the unstained scaffold, which is bright and transparent, good contrast to the stained area is given. The specific stained area in the aggrecan and collagen type I stained images mark the ROIs, which hue information are narrowed in a defined range. For collagen type I the hue range is defined between 3 and 40 as well as between 350 and 358. For aggrecan and collagen type II the hue range is between 10 and 60 as well as 350 and 358. In Figure 6 two histograms are presented that show the hue distribution of two images. Because of the bright color of the staining methods, residues are left on the scaffold that are in the defined hue range of the ROI. The residues are excluded by defining the value range. For collagen type I and aggrecan, the value channel V of every pixel with V > 0.8 was set to zero. The value channel of every other pixel of the image that does not fit into the defined hue range is also set to zero. When converted back to the RGB image, all pixels with V = 0 result in black pixels. The new RGB images are then converted into grayscale images that are binarized into $I(SF)_{edited}$ and $I(CP)_{edited}$ (**Figure 7**) with a small threshold value slightly above 0. Every white pixel now represents the ROI. Since the area of a camera pixel corresponds to approximately 0.42 µm² in the sample, the size of the cell pellet and the area with produced aggrecan or collagen type I can be determined.

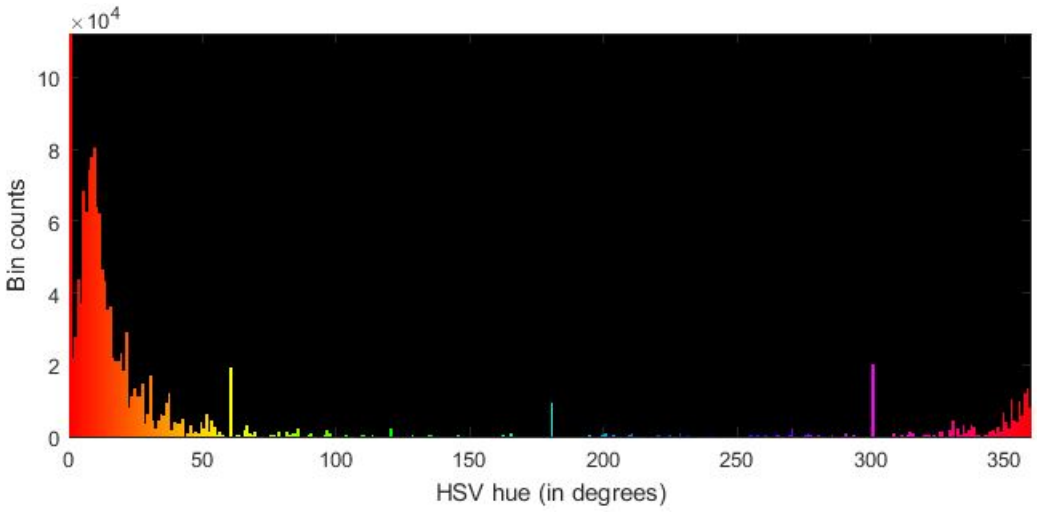

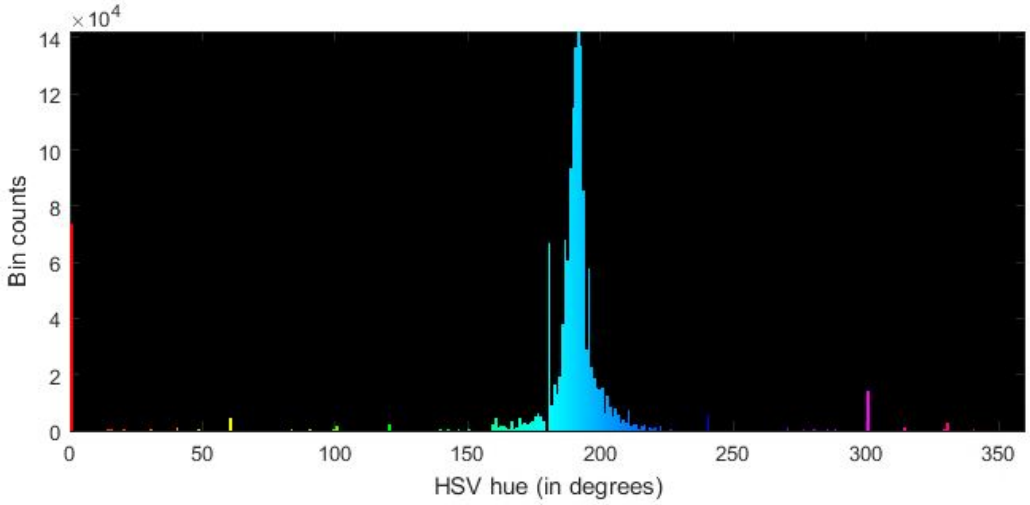

Figure 6: Hue histogram of a collagen type I image (top) and an alcian blue image (bottom).

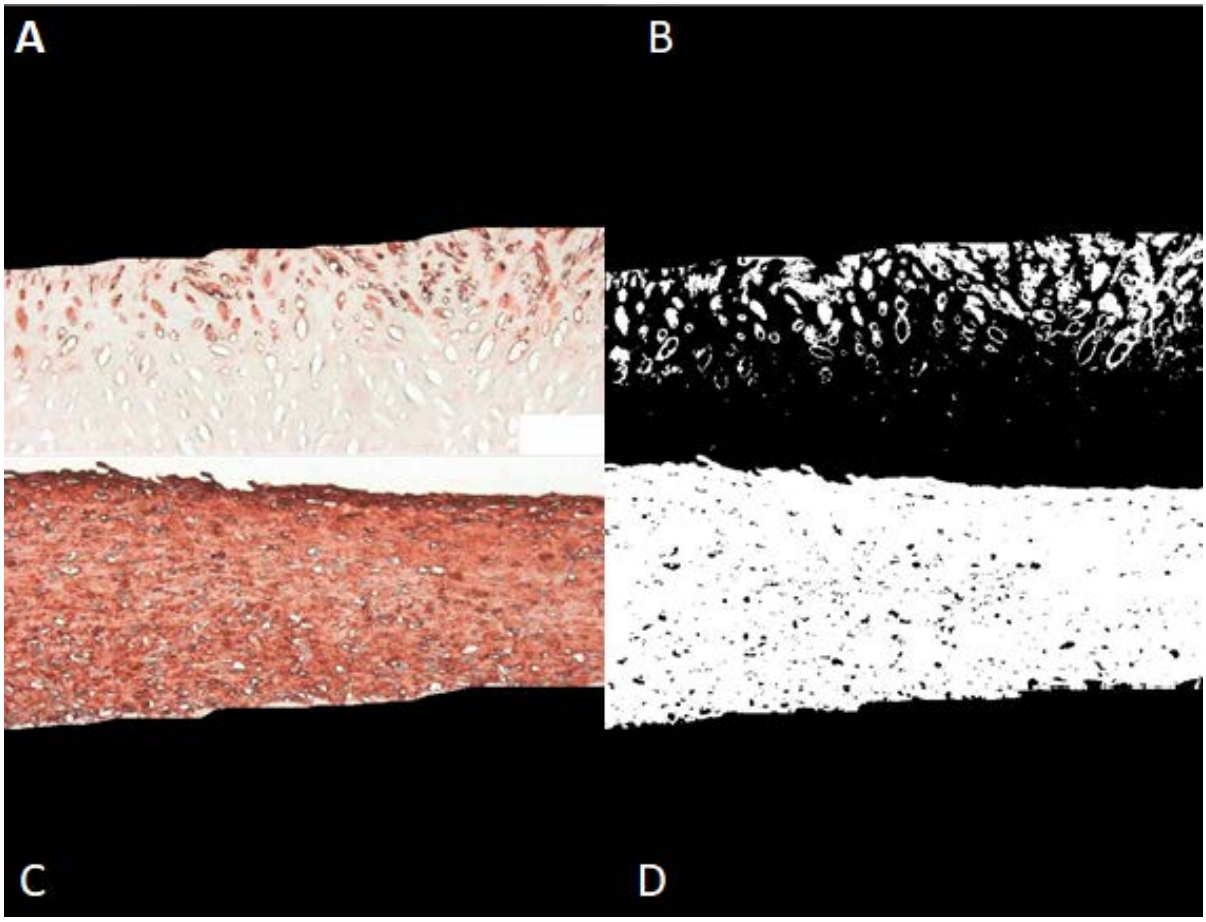

Figure 7: A: Image I(CP) shows the scaffold area with stained collagen type I, B: Image $I(SF)_{edited}$ depicts detected collagen type I in the scaffold as white pixels in the binary image, C: Image I(SF) represents cell pellet area with stained collagen type I, D: Image $I(CP)_{edited}$ illustrates detected collagen type I in the cell pellet as white pixels in the binary image.

2.6 Cell Numbers and Migration Depths

The number of cells inside the scaffold and their migration depths are very important values for the desired engineered cartilage. In order to assess the migration depth of the chondrocytes, cell nuclei have to be identified. Images of preparations stained with alcian blue turned out to be best for the detection of cell nuclei, which are blue stained in every image and overlaid by the other stains. To separate and detect the nuclei in alcian blue images, a range for value and saturation must be defined. The value of every other pixel, which is not in the defined range, is again set to zero. In the binarized image, the cell nuclei are white pixels. Connected regions of white pixels represent a nucleus and are labeled with a connected-component labeling algorithm (MATLAB function *bwlabel)*. First, connected regions are determined using the Moore neighborhood (8 neighbors). Afterwards, distinct numbers are assigned to the regions, which label them in a unique way. For this, the union find algorithm is applied [14]. For determining the important parameter of cell migration depth, the shortest distance from a detected cell nucleus to the surface of the scaffold was calculated. The coordinates of the center of a labeled nucleus are utilized as the position of the cell. The coordinates $E_{x,i}$ and $E_{y,i}$ of the surface line of the scaffold are identified using a canny edge detector (MATLAB function *edge*) [15]. An example is given in **Figure 8**.

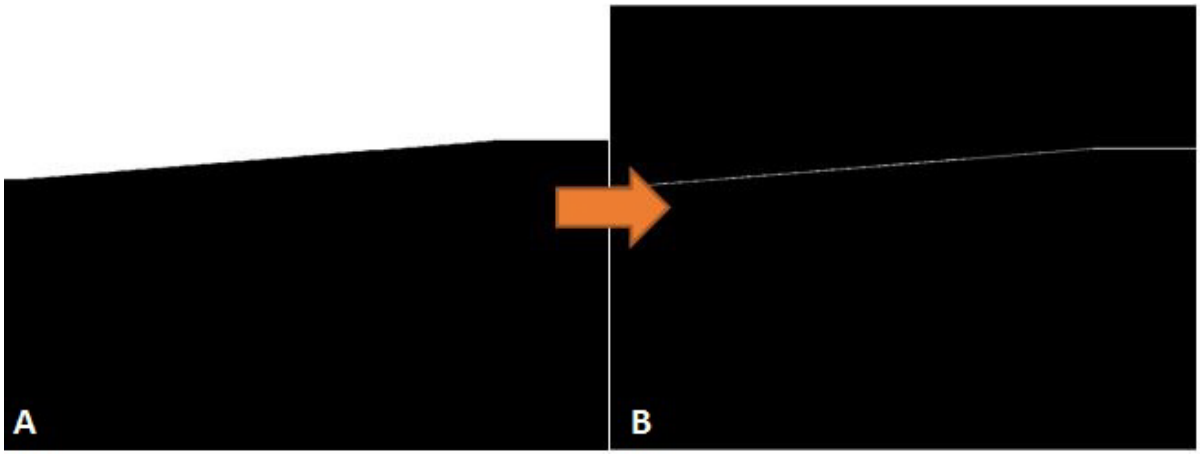

Figure 8: Binary image (A), which represents the scaffold is in black. Using the canny operator, the surface of the scaffold is detected, which results in a new image B.

If N represents the number of white pixels of the edge line, N different distances can be calculated between one nucleus (N_x, N_y) and the edge line pixels $(E_{x,i}, E_{y,i})$ of the surface line:

$$D[i] = \sqrt{\left(E_{x,i} - N_x\right)^2 + \left(E_{y,i} - N_y\right)^2}, i = 1, \dots, N$$

The shortest distance from D[i] is selected as the distance from the nucleus to the surface. **Figure 9** shows the result of the detected nuclei as well as the determined distances to the edge.

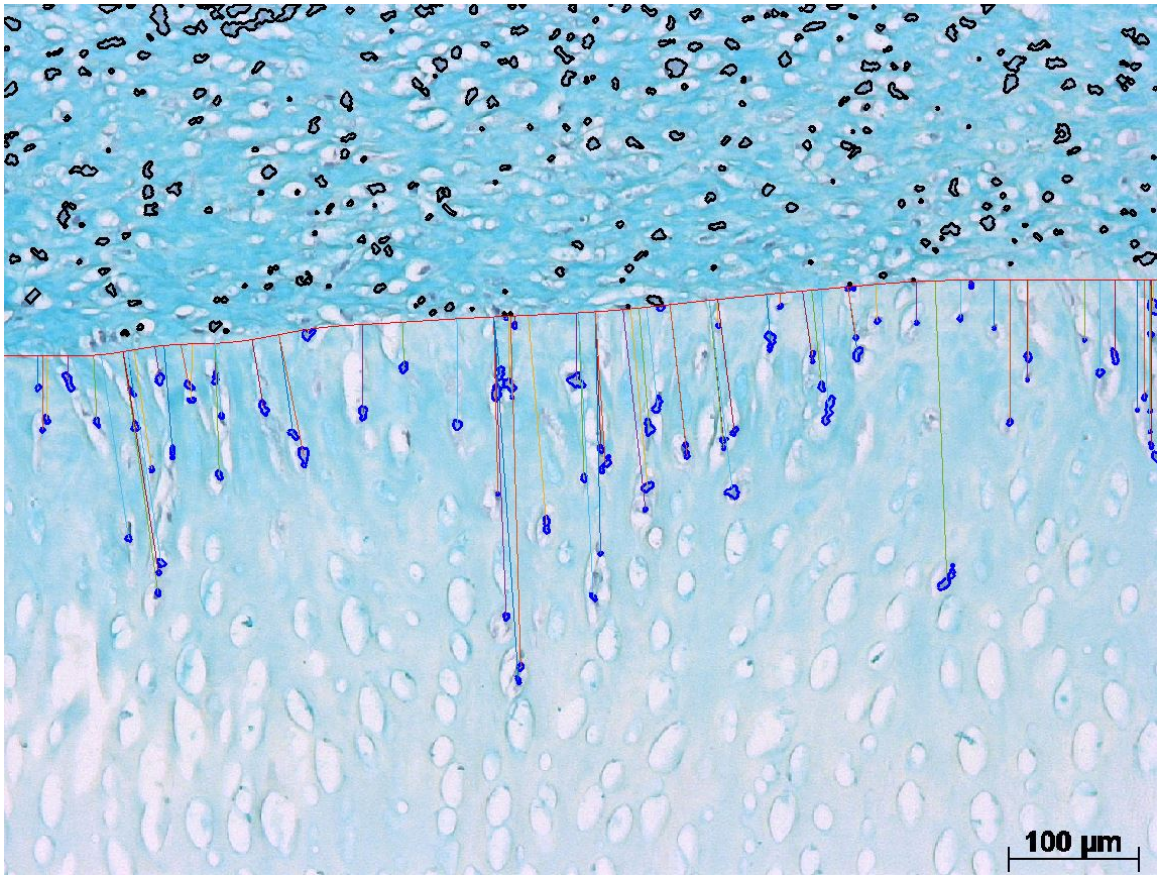

Figure 9: Image of an alcian blue stained sample with detected nuclei in the cell pellet (black framed) and inside the scaffold (dark blue framed). The red horizontal line represents the border between the scaffold and the cell pellet. The lines, which connect the red horizontal line with the nuclei, represent the shortest distances.

2.7 Lacunae Analysis

On the basis that the decellularized scaffold matrix mainly consists of collagen type II, the samples are brown colored after immunohistochemical staining of collagen type II. Because of the high contrast between the brown stained scaffold and the bright lacunae, this staining was employed to determine the orientation and density of the lacunae in the scaffold, which are supposed to influence the cell proliferation and migration. In Figure 10 the principle of lacunae labeling is presented with Figure 10 A as an example. In the binarized and corrected image in Figure 10 C the lacunae can be distinguished. This is done using the major axis of a corresponding ellipse that has the same second moments as the region (MATLAB function *regionprops*). Likewise, the major and minor axis length and the number of pixels of each lacuna are calculated.

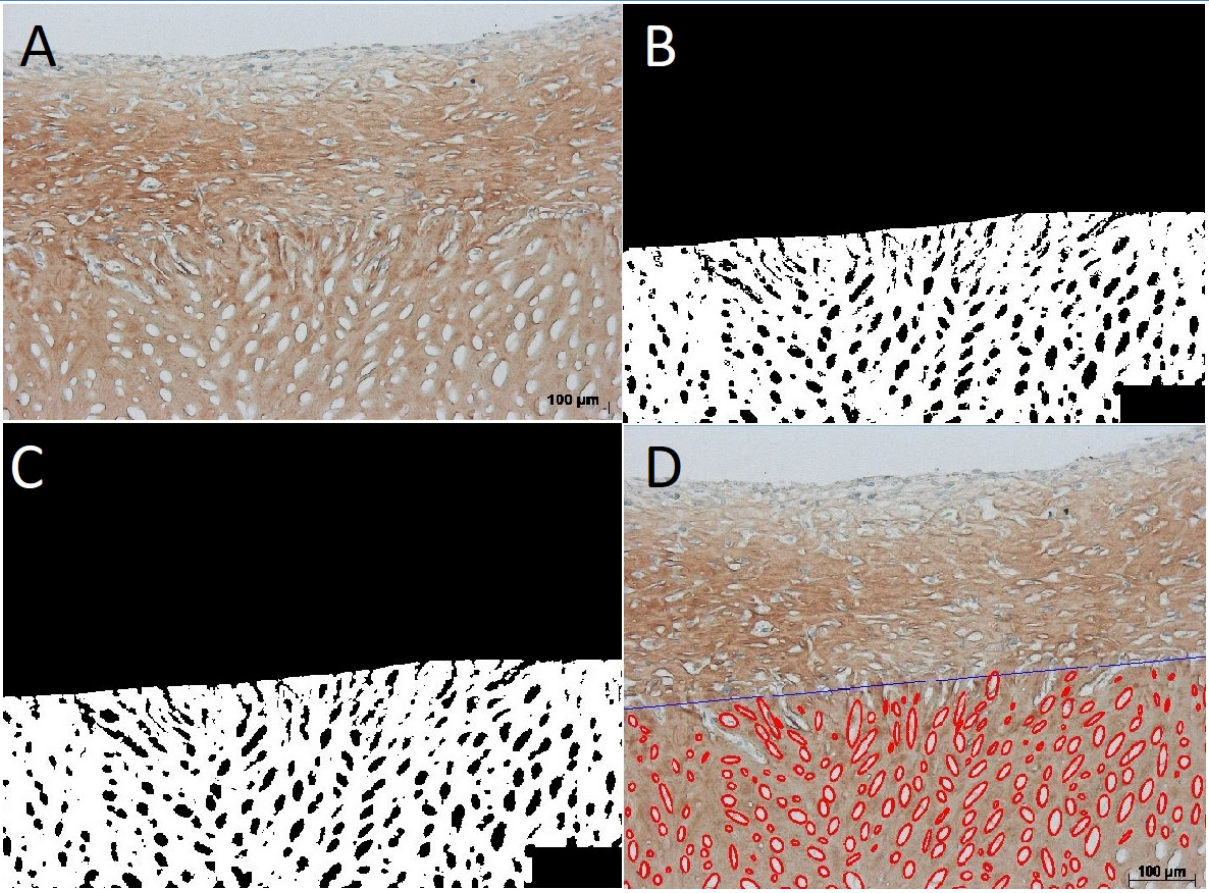

Figure 10: Principle of lacunae detection with original image (A) as an example. Detected lacunae (B) are corrected with erosion and dilatation (C) and labeled as red ellipsis (D).

Since the orientation of the detected lacunae is determined relative to the x-axes of the image, the orientation must be corrected relative to the surface of the scaffold. A straight line is fitted into the surface pixels (MATLAB function *polyfit*), resulting in the slope k of the surface line. The orientation of the lacunae relative to this surface can then be corrected with the slope angle α:

$$\alpha = \arctan(k) \cdot \frac{180}{\pi}$$

3 Results and Discussion

The results of each segmentation algorithm were presented to an expert, who was asked to assess the detected ROIs and results of the software. According to the expert the results of the algorithm were comprehensible and correct. A more precise comparison between the software results and the evaluation of the expert is difficult, because the human expert does not generate quantitative values.

For additional validation of the quality of the results, the outcome has been compared to the results of different conventional laboratory methods. The total number of cells in and on the scaffold was determined with the QuantiFluor dsKits (Promega, Fitchburg; WI, USA) as described in [8]. The total content of Glycosaminoglycans (GAG) in and on the scaffold was measured by the Dimethylmethylene Blue (DMMB) assay [16].

In **Figure** 11 the relation between the detected cell nuclei with the segmentation algorithm and the determined cell number with QuantiFluor assay is presented. A dot represents the average of 6 samples.

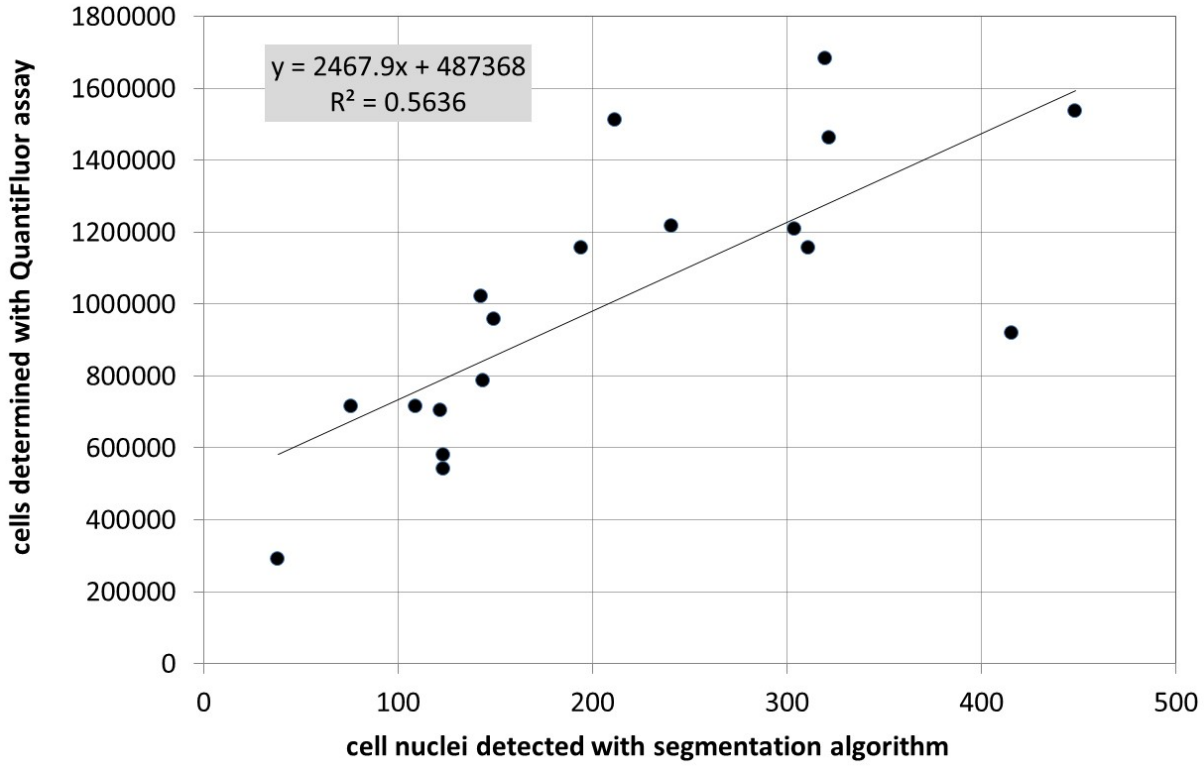

Figure 11: Comparison between the cell count detected by QuantiFluor assay and the number of cell nuclei identified by segmentation algorithm.

A correlation is clearly visible though the correlation coefficient seems not to be very high with $R^2 = 0.5636$. However, it should be considered that these biological samples show a high scatter even within the laboratory results. Additionally, it must be emphasized that the laboratory methods and the algorithms do not evaluate the same samples but only comparable samples, because each scaffold sample can only

be used either for staining or for laboratory analysis, but the same sample cannot be used for a direct comparison of both techniques. Regarding these boundary conditions, the correlation is quite reasonable.

Especially important is the fact, that this image analysis approach is the first method to distinguish between cells in the pellet on the scaffold surface and the much more important cells within the scaffold, which is not possible with the QuantiFluor assay or similar laboratory methods. The differentiation between the cell count in the pellet on the scaffold's surface and the migrated cells inside the scaffold can be important, if different TE methods are compared to improve the migration of the chondrocytes into a scaffold.

Another important value for cartilage quality or chondrocyte differentiation are the glycosaminoglycan (GAG) and aggrecan concentrations, as these polysaccharides and proteins are relevant components of cartilage produced by vital and well differentiated chondrocytes. The DMMB assay gives GAG content in µg per scaffold. The developed algorithm delivers a different value: a relative area in µm² that is stained and detected as aggrecan. If both methods are valid they should exhibit a siginificant correlation. This is depicted in Figure 12.

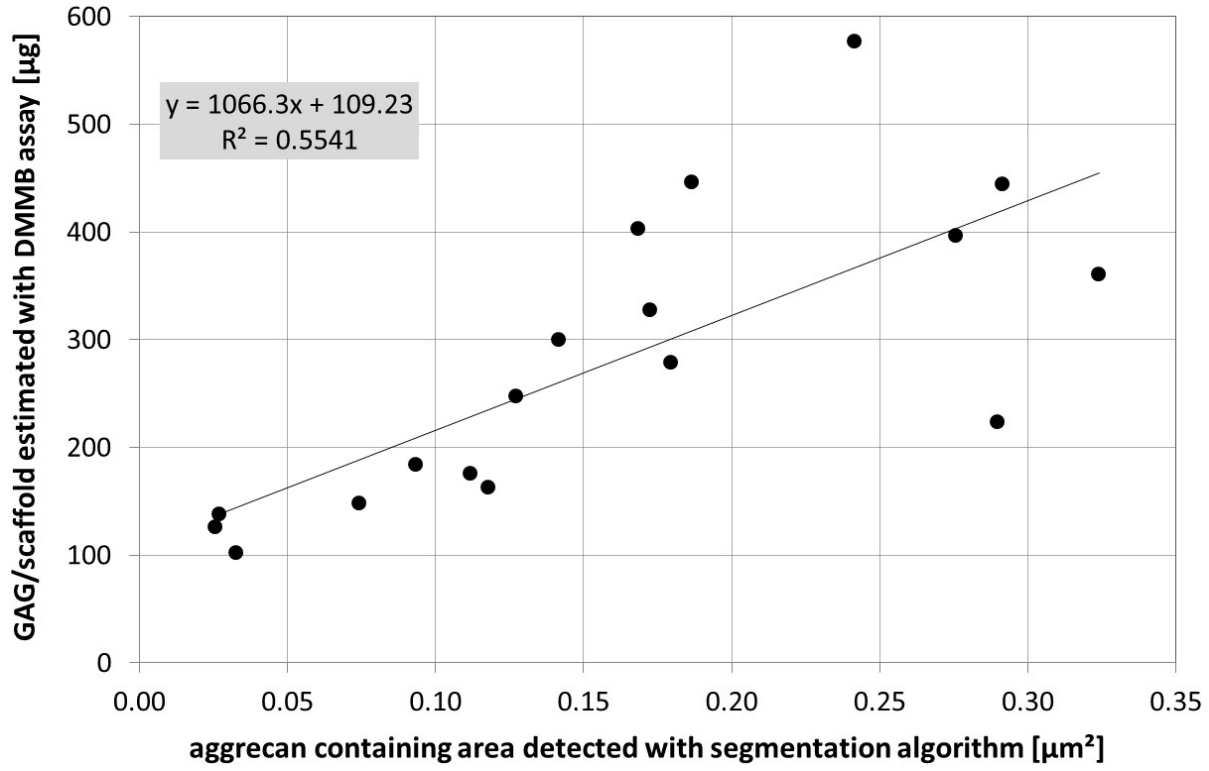

Figure 12: Content of GAG in µg/scaffold determined by DMMB assay in comparison to the aggrecan containing area defined by segmentation algorithm.

It should be repeated that the biological samples are highly variable and both methods were applied to similar but not the same samples. This is an important reason for the seemingly low correlation coefficient of $R^2 = 0.5541$. But even with this restriction there is a pronounced correlation that confirms the algorithm results.

In total 85 different images of three cultivation runs in the bioreactor and three cultivations under static conditions were analyzed with the segmentation algorithm, which is able to determine cell nuclei, aggrecan and collagen I on and in the scaffold separately. Additionally, the orientation, the size and the density of lacunae in collagen type II images is given as well as the migration depth of cell nuclei. For example: In **Figure 9** 253 cell nuclei were detected in the cell pellet and 97 in the scaffold. The average migration depth of the cells is 86 µm while the largest detected distance is 287 µm. **Figure 10** D shows 214 detected lacunae with an average orientation of 57,7° relative to the scaffold surface. This newly obtained data will be analyzed and investigated in more detail in a future paper.

4 Conclusion

This research work presents a novel approach of image segmentation algorithm, which seems to deliver fast and meaningful results for the determination of cell numbers in and on top of the scaffold, migration depths, aggrecan and collagen type I concentrations as well as the number of lacunae and their orientation relative to the scaffold´s surface. To our knowledge, it is the first and only semi-automatic technique that determines migration depths and lacuna properties. It also seems to be the first segmentation algorithm, which separates the detection of cell nuclei, aggrecan and collagen type I between scaffold and cell pellet. The algorithm will be employed to support the assessment of cultivation methods and conditions. Further investigation will be performed to find out if the density, the size and the orientation of the lacunae have an influence on cell migration and growth. More images will be analyzed to validate the results of the algorithm, which will be also refined to improve the reliability of the method.

References

[1] N. Rotter, M. Bücheler, A. Haisch et al., “Cartilage tissue engineering using resorbable scaffolds,” *Journal of Tissue Engineering and Regenerative Medicine*, vol. 1, no. 6, pp. 411–416, 2007.

[2] A. Salerno, E. Di Maio, S. Iannace et al., “Tailoring the pore structure of PCL scaffolds for tissue engineering prepared via gas foaming of multi-phase blends,” *Journal of Porous Materials*, vol. 19, no. 2, pp. 181–188, 2012.

[3] S. J. Hollister, “Porous scaffold design for tissue engineering,” *Nature Materials*, vol. 4, no. 7, pp. 518–524, 2005.

[4] S. Schwarz, L. Koerber, A. F. Elsaesser et al., “Decellularized cartilage matrix as a novel biomatrix for cartilage tissue-engineering applications,” *Tissue Engineering. Part A*, vol. 18, 21-22, pp. 2195–2209, 2012.

[5] M. N. Gurcan, L. E. Boucheron, A. Can et al., “Histopathological image analysis: A review,” *IEEE Reviews in Biomedical Engineering*, vol. 2, pp. 147–171, 2009.

[6] J. M. Haggerty, X. N. Wang, A. Dickinson et al., “Segmentation of epidermal tissue with histopathological damage in images of haematoxylin and eosin stained human skin,” *BMC Medical Imaging*, vol. 14, p. 7, 2014.

[7] T. J. Fuchs and J. M. Buhmann, “Computational pathology: Challenges and promises for tissue analysis,” *Computerized Medical Imaging and Graphics*, vol. 35, no. 7, pp. 515–530, 2011.

[8] G. Matheron, *Random sets and integral geometry*, Wiley, New York, 1975.

[9] S. Princz, U. Wenzel, H. Tritschler et al., "Automated bioreactor system for cartilage tissue engineering of human primary nasal septal chondrocytes," *Biomedizinische Technik. Biomedical Engineering*, vol. 62, no. 5, pp. 481–486, 2017.

[10] S. Princz, U. Wenzel, S. Schwarz et al., "New bioreactor vessel for tissue engineering of human nasal septal chondrocytes," *Current Directions in Biomedical Engineering*, vol. 2, no. 1, p. 1415, 2016.

[11] A. F. Elsaesser, C. Bermueller, S. Schwarz et al., "In vitro cytotoxicity and in vivo effects of a decellularized xenogeneic collagen scaffold in nasal cartilage repair," *Tissue Engineering. Part A*, vol. 20, 11-12, pp. 1668–1678, 2014.

[12] A. F. Elsaesser, S. Schwarz, H. Joos et al., "Characterization of a migrative subpopulation of adult human nasoseptal chondrocytes with progenitor cell features and their potential for in vivo cartilage regeneration strategies," *Cell & Bioscience*, vol. 6, p. 11, 2016.

[13] K. ElDahshan, M. Youssef, E. Masameer et al., "Comparison of Segmentation Framework on Digital Microscope Images for Acute Lymphoblastic Leukemia Diagnosis Using RGB and HSV Color Spaces," *Journal of Biomedical Engineering and Medical Imaging*, vol. 2, no. 2, 2015.

[14] R. Sedgewick, *Fundamentals, data structures, sorting, searching*, Addison-Wesley, Boston, Mass., 2009.

[15] J. Canny, "A computational approach to edge detection," *IEEE Transactions on Pattern Analysis and Machine Intelligence*, vol. 8, no. 6, pp. 679–698, 1986.

[16] I. Barbosa, S. Garcia, V. Barbier-Chassefière et al., "Improved and simple micro assay for sulfated glycosaminoglycans quantification in biological extracts and its use in skin and muscle tissue studies," *Glycobiology*, vol. 13, no. 9, pp. 647–653, 2003.

SOCIETY FOR SCIENCE AND EDUCATION UNITED KINGDOM

JBEMi JOURNAL OF BIOMEDICAL ENGINEERING AND MEDICAL IMAGING

ISSN: 2055-1266

Radio Frequency Ablation of Liver Tumor
-Influence of Large Vessels location and vein wall

[1]Md.Mohaiminul Islam, [2]Muhammad Asadul Islam
[1,2]Bangladesh University of Engineering and Technology, Bangladesh;
[1]mishkat1096@gmail.com; [2]asadbuet2041@yahoo.com

ABSTRACT

Radiofrequency ablation (RFA) is a process that uses RF energy which is one form of electromagnetic energy to destroy cancer cells. This is a minimally invasive technique to treat some kinds of cancer and can be applied to nonsurgical patients. The frequency range of RF current is between 300 kHz to 1 MHz. Tumors from lung, liver, kidney and bone may be removed by performing RFA. Here in our model a patient specific simulator for Radiofrequency ablation (RFA) of liver tumors has been developed and the effects of the presence of blood vessel inside the liver tissue on the temperature distribution and the volume of ablation has been shown. And the effect of temperature distribution on the distance between large blood vessel and electrode tip has been shown, all these effects has been shown for two different models one is with vein wall and one without vein wall. Heat is generated within liver tumors utilizing RF energy from RF current where the RF current is generated using a power generator. With the heat generation, the tissue temperature reaches a temperature where cell death occurs. This cell death occurs when the cells are heated to approximately 50 °C or above. Temperature should not exceed 100 °C because it will cause overheating. We develop the model using ANSYS 16.2 and numerically solve the problem to view the variation of temperature around the electrode tip within the liver tissue. We consider a model with blood flow inside a vessel and which is in the vicinity of the heated tissue and a model without a vessel.

Keywords: RFA , vein, blood vessel,electrode .

1 Introduction

Liver cancer, also known as hepatic cancer and primary hepatic cancer, is cancer that starts in the liver [1] . Cancer which has spread from elsewhere to the liver, known as liver metastasis, is more common than that which starts in the liver [2]. Primary liver cancer is globally the sixth most frequent cancer (6%) and the second leading cause of death from cancer (9%) [3][2]. In 2012 it occurred in 782,000 people and resulted in 746,000 deaths [3]. There are many possible treatments for liver cancer which include surgical resection, liver transplantation, microwaves, lasers, cryotherapy and finally RFA. Surgical resection has an increased risk of complications such as liver failure and also depends on some factors such as tumor size, multifocal diseases and position of the tumor. In cryosurgery liquid Nitrogen is used to freeze the tumor tissue and thus destroys the tumor tissue. Liver transplantation requires a donor having a blood type that matches or is compatible with the recipient's. Microwave ablation is also a promising technique but

DOI: 10.14738/jbemi.46.3261
Publication Date: 8th December 2017
URL: http://dx.doi.org/10.14738/jbemi.46.3261

currently RF is the most dominant treatment model as microwaves for ablation have to make an approach with commercial and academic developments with less invasive and easier to use technique.

2 Background

RFA is a widely accepted method for treating liver cancer tumors, as it offers a less invasive alternative compared to traditional surgical resection and is the method of choice for a large number of patients. Surgical resection involves a major surgical operation that isn't suitable for all patients due to multifocal disease, tumor size and location of tumor in relation to key vessels [4]. RFA can be used for a greater number of patients and it has a greater potential in repeated treatment of tumor recurrences or new metastases compared to traditional surgical resection [5]. Although RFA is commonly used for many patients, surgical resection still is the method with highest long-term survival rates [6]. This fact might partially be a result of the high recurrence rates related to RFA which is a result of surviving tumor cells close to large vessels due to the heat sink effect [7]. The liver is an organ with very high blood perfusion; blood is supplied from two large vessels, the hepatic artery and the portal vein. Large veins branching from the portal vein can be found throughout the whole liver. Numerous both experimental and numerical modelling and simulation studies have been performed to investigate the nature of RFA in liver tissue, several of these studying the effects of blood perfusion. The numerical approach is a common and popular method of studying RFA. It is both fast and inexpensive compared to experimental studies; this makes it a powerful tool both for investigating difficulties related to RFA and for the tryouts of new approaches for improving the method total occlusion. Kolios et al. showed by a numerical simulation study that microvascular perfusion of tissue plays a significant role in altering the amount of heat transferred to large vessels, where an increased perfusion decreases the cooling effect from large vessels [8]. Different approaches of decreasing blood perfusion in order to decrease the heat sink effect have been investigated; vascular occlusion due to clamping and pharmacological decrease of blood flow has both been shown to give an increase in ablation volume. According to Gilliam's will a decreasing blood flow decrease the cooling effects of perfusion but also increase the risk of vessel injuries due to ablation [9].

3 Equipment and Methods

3.1 Power Generator

The radiofrequency generator supplies RF current at a frequency at about 500 kHz and this RF current is then applied to the patient's target tissue. Then this current flows through the patient's target tissue and then back to a ground pad which is placed on patients back or thigh. As this current always changes its direction, the ions in the area of target tissue try to follow the changes in direction of the current. Therefore, for their movement a joule heating effect is obtained around the electrode. Power output for different power generators lies between 60 W and 250 W.

Figure 1 RF generator (upper left), cooling fluid pump (right) and three cool-tip single straight electrodes [10]

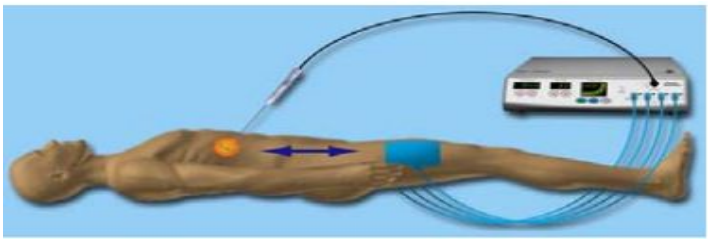

Figure 2 Application of RFA process

3.2 Electrode

Different types of electrode can be used in RFA.

1. Plain electrode
2. Cooled electrode
3. Wet electrode
4. Expandable electrodes
    I. Multitined electrodes
    II. Coiled electrodes
5. Bipolar Electrodes

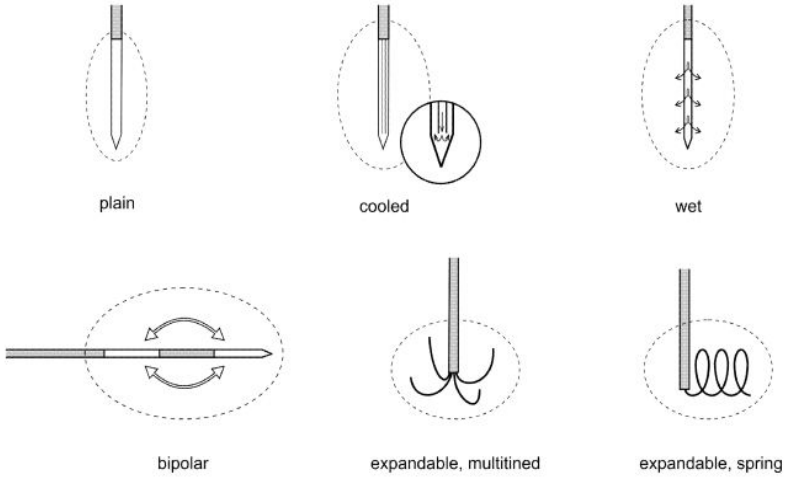

Figure 3 Different types of electrodes used in RFA

In this work, we consider a cooled electrode which has cool tip. The RF generator is supplying RF current to the cool-tip electrode which has a needle like internally cooled geometry. An external pump is used to pump cooling fluid. Cooling is done to ensure the deployment of more power into the whole tissue compared to a non-cooled electrode and thus cooling protect the tissue near the electrode from charring. Electrolyte solution can be injected into the tissue to improve thermal conductivity. But this is difficult to model.

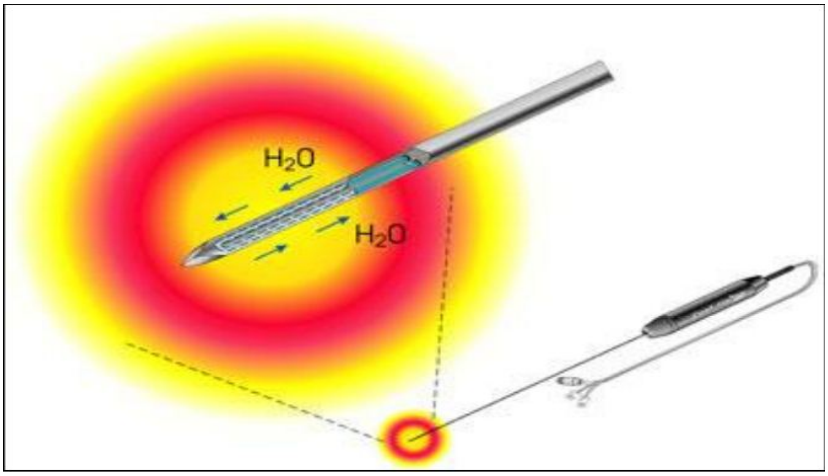

Figure 4 the Cool tip RF system [11]

Tissues can hold their stability functions upto about 40 °C but thermal injury can be occurred at any temperature above 43 °C. Irreversible cell damage will occur in a few seconds if temperature is kept higher than 50° – °55 C for around 5 minutes. Instantaneous cell death will occur if temperature is kept between 60 °C and 100 °C . Temperature should be kept within 100 °C because overheating occurs above this temperature which vaporizes and carbonizes the tissues that produces an insulated layer on the electrode surface and the volume of the tissue which can be treated is largely compromised [12]. The frequency of RF Current is kept around 500 kHz and the voltage is 80 V.

4 Principles of Heat Transfer and RF Tissue Heating

Here heat transfer takes place by two mechanisms: conduction and convection. Radiation can be ignored [13].

4.1 Conduction

Fourier's law of conduction is

$$q = -k\frac{\partial T}{\partial x} \tag{1}$$

Where q [W m^{-2}] is the heat flux, k [W m^{-1} K^{-1}] is the thermal conductivity and x is the direction of temperature gradient.

Fourier's law together with the first law of Thermodynamics gives the general heat conduction equation. The following equation will help us to know the spatial and time dependent changes of the temperature field in a heat transferring medium.

$$\rho C\ \frac{\partial T}{\partial t} + \nabla\ \cdot (-k\nabla T) = Q \tag{2}$$

Here ρ [kg m^{-3}] is the medium's density, C [J kg^{-1} K^{-1}] is the medium's heat capacity and Q [W m^{-3}] is either a heat source or sink.

4.2 Convection

Here a convective term is added to the general heat conduction equation to represent the convective heat transfer within the flowing medium.

$$\rho C\frac{\partial T}{\partial t} +\ \nabla\ \cdot (-k\nabla T +\ \rho C\mathbf{u}T) = Q \tag{3}$$

Here **u** [m s^{-1}] is the velocity field vector of the flowing fluid.

Again Newton's law of cooling represents the convective heat transfer from a medium to a fluid.

$$q_s = h(T_s - T_\infty) \tag{4}$$

Here h [W m^{-2} K^{-1}] is the heat transfer co-efficient which depends on material property, geometry and motion of the fluid flow and on fluid properties.

4.3 Bio-heat transfer

Heat transfer in tissue is also affected by the blood perfusion. Convection occurs between solid tissue and flowing blood for blood vessel of all sizes. Vessel size, flow velocities and number of vessels in the volume of interest have impact on the convection between tissue and blood. Pennes Bio-heat equation adds blood perfusion and generated metabolic heat terms in general heat conduction equation.

$$\rho C\frac{\partial T}{\partial t} = \nabla \cdot (k\nabla T) - m_b C_b (T - T_b) + Q_m \tag{5}$$

Where m_b, C_b and T_b is mass flow rate, specific heat and temperature of the blood respectively [14]. Q_m is the heat generated in the metabolic process and this is negligible [15]. It is assumed in the Pennes Bio-

heat equation that all the heat transfer between tissue and blood occurs in the capillary bed that means capillary blood flow act as a heat sink [16].

4.4 RF tissue heating

RF tissue heating is based on the principle of inducing an ion current into tissue by the application of a RF field between an electrode and a grounding pad. The friction that ion movement in the tissue causes results in so-called joule heating (resistive heating). Biological tissues can be treated as quasi-static in the RF range (300kHz – 1Mhz), this means that they can be described as purely resistive, neglecting the small part of impedance that dielectric permittivity constitutes. Electric field, E [V m-1], applied to a tissue can be described by Laplace's equation:

$$-\nabla(\sigma\nabla E) = -\nabla\sigma E = 0 \tag{6}$$

Where σ (S/m) is the electrical conductivity, V (V) is the potential and ∇ the gradient Operator. The electrical conductivity σ is the ability of a material to carry the flow of an electric current and depends on concentration of the ions, temperature of the solution, specific nature of the ions. Conductivity value also depends on time and temperature.

Although the exact behavior of σ dependency of temperature in tissues in unknown, for temperature ranges around body temperature the electrical conductivity increases linearly; when 100º C are achieved in the tissue, boiling and vaporization will occur, and thus raise of tissue impedance and insulating effects of gas bubbles, leading to an electrical conductivity decrease .

Moreover, the determination of the electrical conductivity is a rapid and convenient means of estimating the concentration of ions in solution [17].

The Ohm´s law demonstrates the relation between current flux J, the intensity of the electric field E and the electrical conductivity:

$$\mathrm{J} = \sigma \mathrm{E} \tag{7}$$

where J is the current density (A/m^2) and E is the electric field intensity (V/m).

The product of current density J and electric field intensity E generates the power density.

4.5 Fluid flow type

Fluid flow are of two types: turbulent and laminar. When the fluctuations of velocity are random it is turbulent flow and the fluctuations of velocity don't occur, it is laminar flow [18]. The Reynolds number is an important parameter to determine whether a flow is laminar or turbulent. When Reynolds number is less than 2300, the flow is laminar and any value greater than 4000 is turbulent. This are valid for flow in pipes. Reynolds number for a pipe can be expressed by the following equation

$$Re = \frac{\bar{u}D}{v} \tag{8}$$

Here D is the diameter of the pipe, ū is the mean velocity and v is the kinematic viscosity.

The blood flow in human body is laminar. It can be seen from the velocity profile which is parabolic in shape with v=0 at the vessel wall and highest at the center of the stream. So the energy losses in the flowing blood is reduced due to the orderly movement of the adjacent layer of blood flow [19].

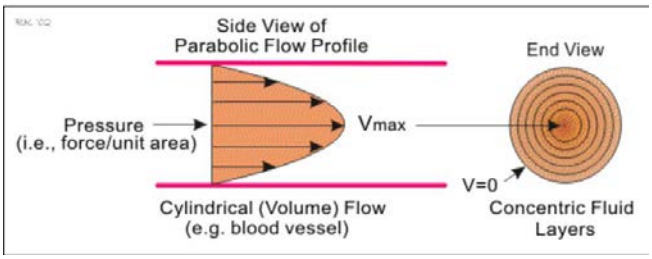

Figure 5 Parabolic flow profile[19]

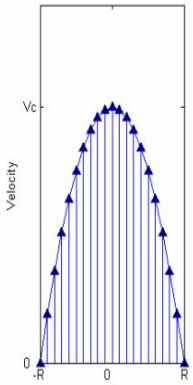

Figure 6 Fully developed laminar velocity profile

5 RFA modelling with ANSYS

5.1 Geometry and materials properties

5.1.1 Liver

The liver tissue is assumed cylindrical in shape. The diameter of the cylinder is 50 mm and height is 100 mm. Thermal conductivity of perfused liver is 2.18 W m^{-1} K^{-1}[20] The material properties of the liver tissue is shown in the figure below:

Name	*Symbol*	*Unity*	*Value*
Density	ρ	kg/m^3	1,060
Specific heat	C	J/kg·K	3,600
Heat conductivity	k	W/m·K	0.512
Resistivity	σ	Ω·m	3.003

Figure 7 Thermal and electrical properties of liver [21]

5.1.2 Blood and vein

The vein is hollow cylindrical with a diameter of 4 mm and the thickness of the vein is 0.5 mm. The blood flows inside the vein. The property for blood and vein is given in the figure below:

Property	**Symbol**	**Value**
Density of blood	ρ_b	1050 kg/m^3
Dynamic viscosity of blood	μ_b	0.0035 kg/m·s
Density of vein wall	ρ_w	1120 kg/m^3
Specific heat of blood	C_{pb}	3820 J/kg°C
Specific heat of vein wall	C_{pw}	3780 J/kg°C
Thermal conductivity of blood	K_b	0.492 W/m·K
Thermal conductivity of vein wall	K_w	0.56 W/m·K

Figure 8 Material property of blood and vein [22].

5.1.3 Electrode

The electrode has two parts, electrode base and electrode tip. The electrode base is made of plastic. The electrode has a height of 90 mm. and diameter of 2 mm.

Constant	Value
Electrode electrical conductivity	7.4e6 S/m
Electrode thermal conductivity	15 W/m·K
Electrode density	8000 kg/m^3
Electrode specific heat	480 J/kg·K
Plastic electrical conductivity	1e-5 S/m
Plastic thermal conductivity	0.026 W/m·K
Plastic density	70 kg/m^3
Plastic specific heat	1045 J/kg·K

Figure 9 Material property of electrode [23]

All the parts are sketched in Solidworks 2016 and assembled to get the final assembly.

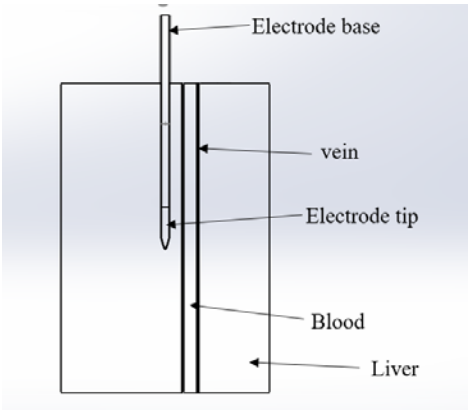

Figure 10 Schematic view of the model (with vein wall)

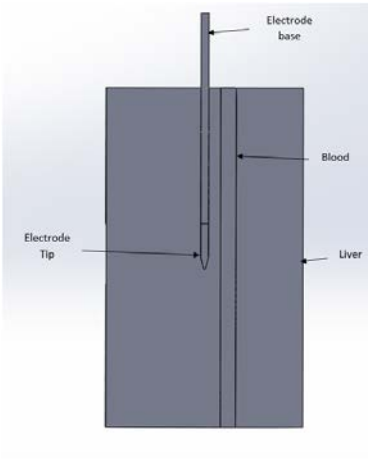

Figure 11 Schematic view of the model (without vein wall)

5.2 Mesh

The principal concept of FEM is to divide a region (1D, 2D or 3D), over which a certain physical behavior and differential equation is valid, into smaller elements. A region divided into elements is called mesh. The mesh element for a 1D-region constitutes of linear segments where the end points constitute the nodes of the mesh. For 2D, triangular shaped mesh elements can be used where the three corners constitute the nodal points. For 3D, tetrahedrons can be used as mesh elements where the four corner points constitute the nodes [24]. Both for 2D and 3D cases other geometries then the above mentioned can be used as mesh elements, such as rectangular- and box like geometries. The number of elements that the region of interest is divided into will partly steer the accuracy of the solution, where more mesh

elements offers a more accurate approximation. An increase in the number of mesh elements also increases the size of the equation system that has to be solved.

The mesh size in the liver was set to increase smoothly from the middle of the model to the outer boundary so that we keep a finer mesh around the electrode and the vessel but a coarser one in the liver external walls. It is important to set a slow transition between the center of the model to the its boundaries in order to prevent numerical instabilities. Details of mesh analysis is described in appendix 1.

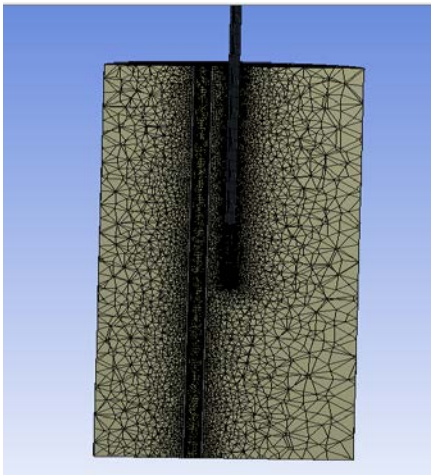

Figure 12 (a) Schematic view of the mesh distribution (sectional view)

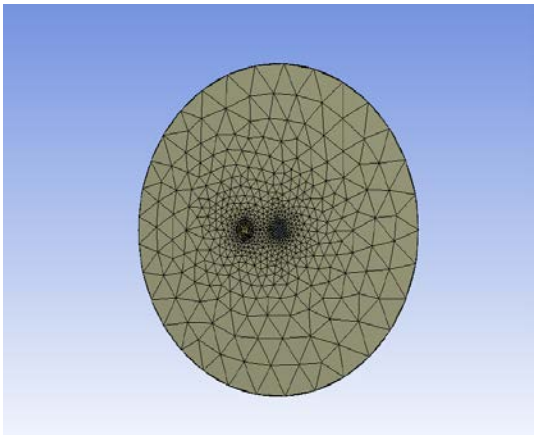

Figure 12 (b) Schematic view of the mesh distribution.(top)

5.3 Boundary conditions (BCs)

The geometry is divided into so called sub-domains that are regions separated by boundaries. It is very important to impose correct computational domains and boundary conditions for not affecting the accuracy of the results. Once the boundary conditions for all domains (liver and vessel) are set correctly, it is possible to launch the simulation.

The outer boundaries of the liver and the inlet of the blood vessel are modeled with a Dirichlet condition of 37° C equal to the body temperature.

The symmetry plane is set with the condition of zero heat flux (Newman condition) and the blood flow velocity has been randomly set at a low value of 2mm/s.

According to the operating principle of the Cool-tip electrode and to the Dirichlet conditions, the convective cooling by fluid flow is large enough to guarantee a constant temperature on the outer surface of the electrode. Moreover, measurements done by Welp et al. in ex vivo experiments on liver tissue with a cool-tip 2 mm electrode, demonstrated that for the entire duration of the thermal treatment the tip electrode temperature were almost constant at 10°C.Based on that, the assumption for the temperature electrode wall is equal to 10° C.

Table 1 for boundary conditions

Domain	Boundary Conditions
vein	Initial temperature 37°C
blood	Initial temperature 37°C and velocity 2mm/s
liver	Initial temperature 37°C
electrode	Temperature fixed at 10°C and fixed 80V at electrode tip

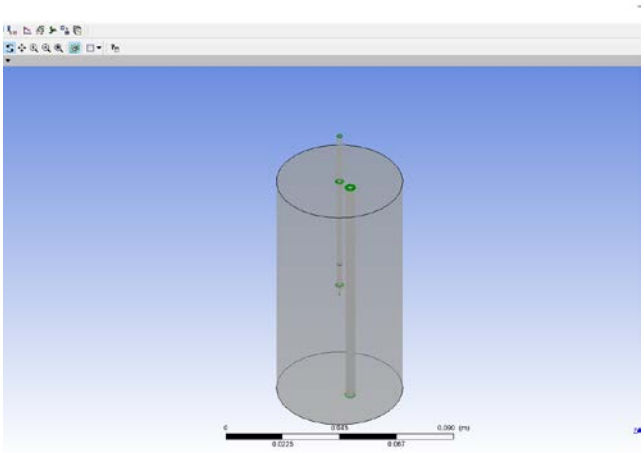

Figure 13 Shows different domains

6 Result

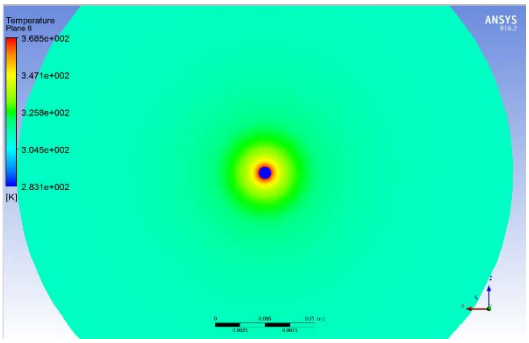

Figure 14 shows the unaffected symmetrical ablation volume which is created when no large blood vessel is present in the model

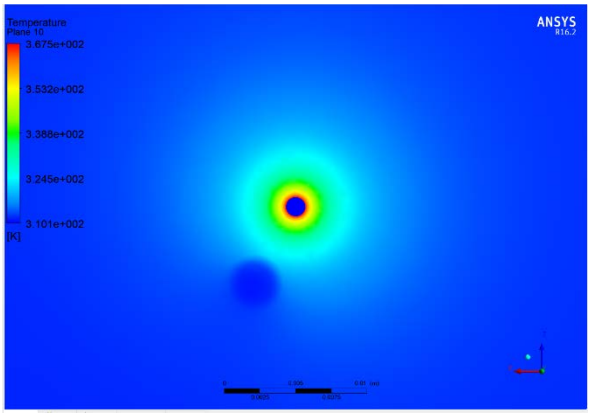

Figure 15 shows the impact of large blood vessel considering no vein wall (6 mm from electrode)

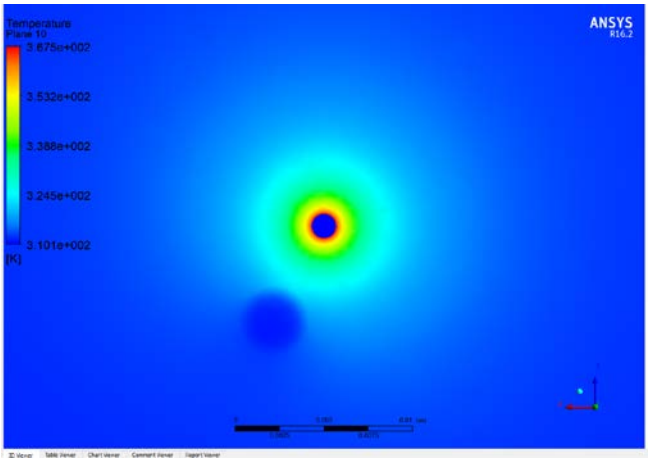

Figure 16 shows the impact of large blood vessel considering vein wall (6 mm from electrode)

In this model the blood vessel of 4mm diameter was 6mm from electrode (center to center) .It can be seen that maximum temperature in the absence of blood vessel was a little higher. And ablation zone was larger in the absence of blood vessel. Both can be described by heat sink effect of large blood vessel. For 6mm distance of large vessel, presence of vein wall had no effect. And temperature distribution was symmetric. For effective RFA modelling It was necessary to set an assumption - Ablative temperature less than 100° C to be maintained constant during the therapy;

Because temperature higher than 100° C causes vaporization, carbonization, charring of tissue and cause to increase impedance. Taking into account both assumptions and considering the initial temperature value (body temperature of 37° C) in the model, it was possible to define an ideal curve.

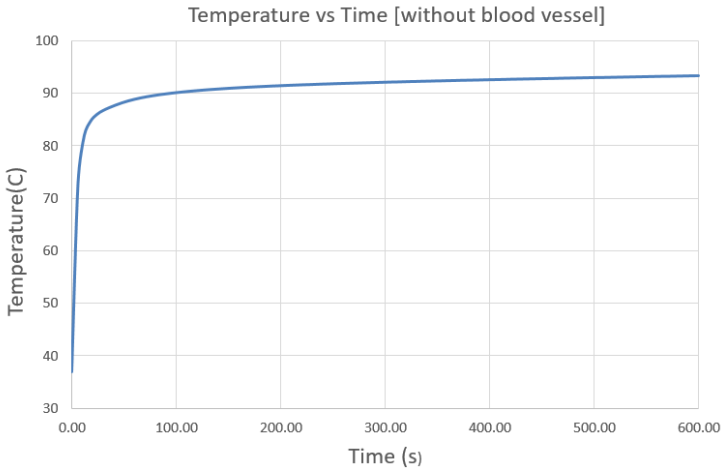

Figure 17 shows variation of temperature with time at electrode tip (doesn't contain blood vessel)

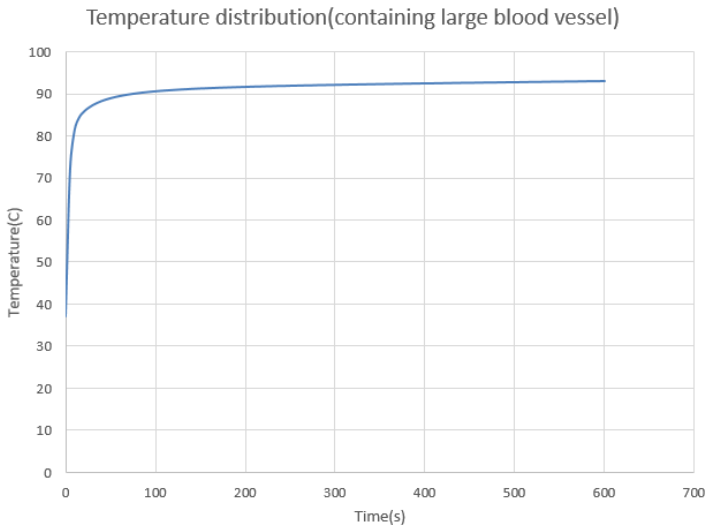

Figure 18 shows variation of temperature with time at electrode tip (containing large blood vessel 6mm from electrode)

Figure 5.12 was obtained keeping blood vessel at 6mm from electrode in both cases (considering vein wall and not considering vein wall) gave same temperature distribution. Temperature distribution was uniform throughout.

Similar simulation was done using COMSOL and the result is following graph.

SOURCE https://www.comsol.com/model/download/326381/models.heat.tumor_ablation.pdf

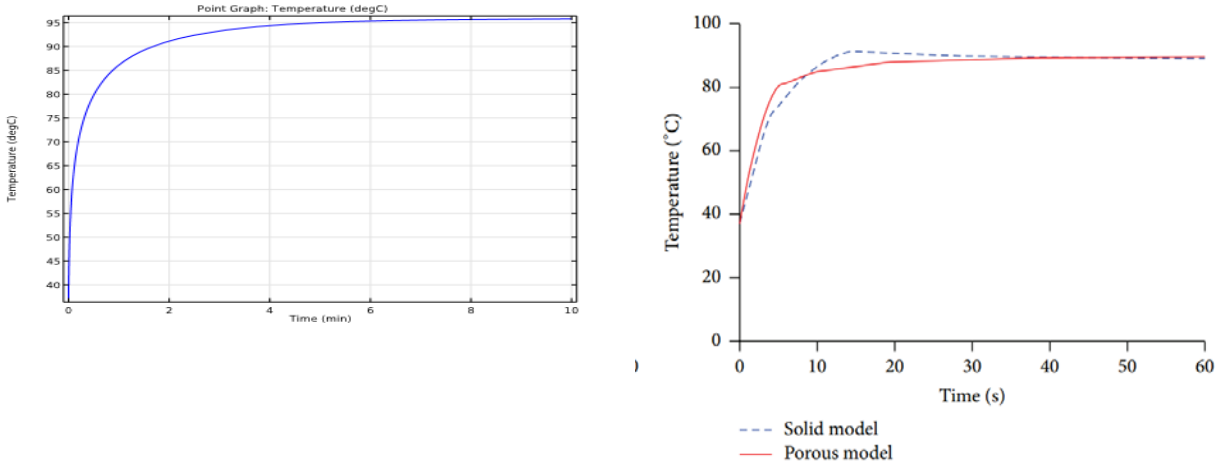

(Similar results were obtained by Montree Chaichanyut and Supan Tungjitkusolmun in 2016 [25])

To find the effect of large blood vessel location, position of the blood vessel was changed to 5mm from electrode and figure 5.13 and 5.14 was obtained.

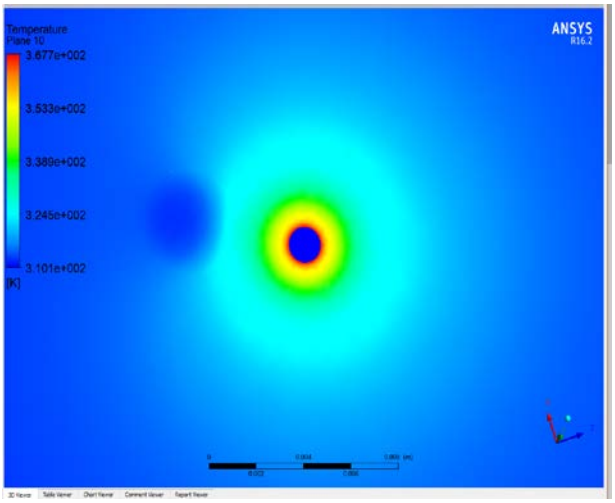

Figure 19 shows the impact of large blood vessel not considering vein wall (5 mm from electrode)

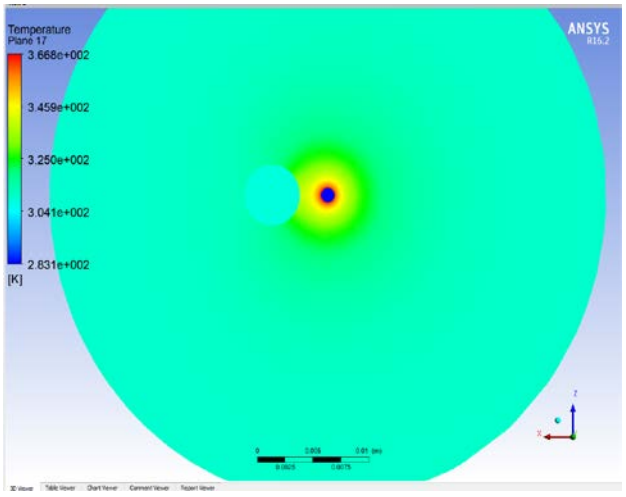

Figure 20 shows the impact of large blood vessel considering vein wall (5 mm from electrode)

An interesting observation in this simulation was, though temperature was lower at vessel side when we didn`t consider vein wall it changed when we considered vein wall. Temperature was higher at vein wall than other side.

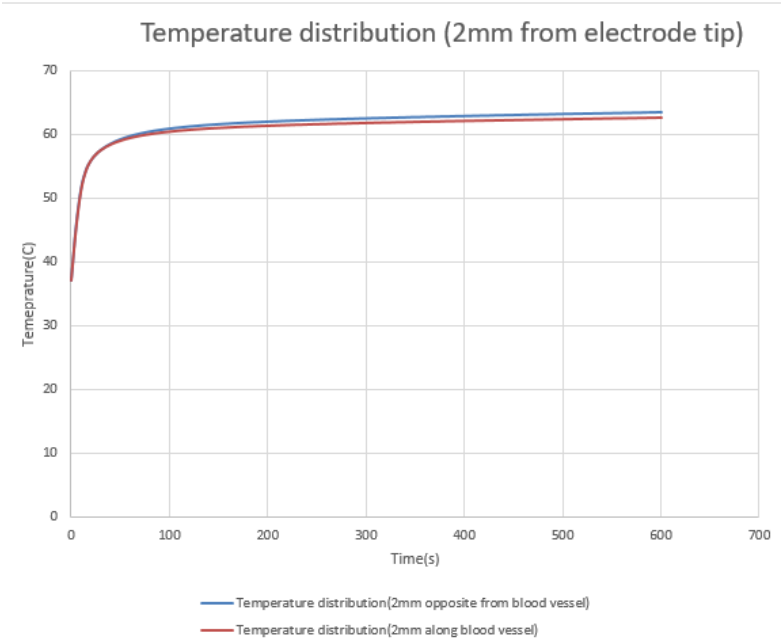

Figure 21 Shows variation of temperature between equally spaced (2mm) one in blood vessel side and another on the opposite side (not considering vein wall).

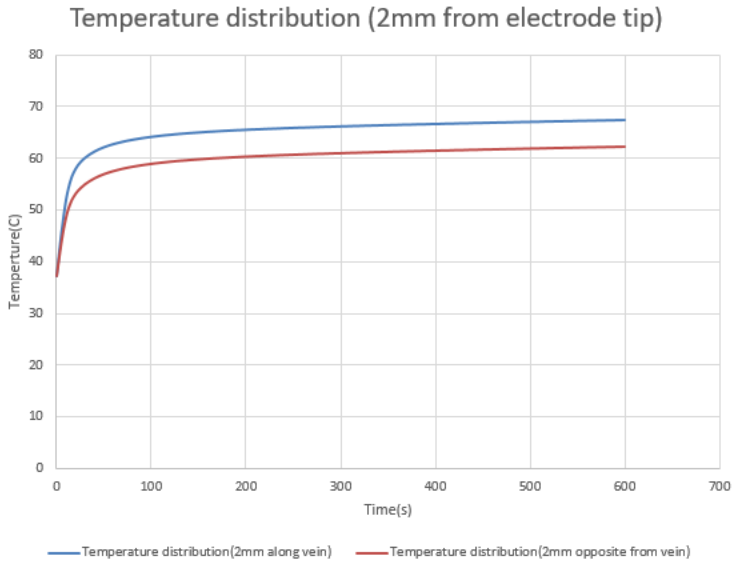

Figure 22 shows variation of temperature between equally spaced (2mm) one in blood vessel side and another on the opposite side (considering vein wall).

Figure 4.15 & Figure 4.16 shows temperature distribution 2mm from electrode one considering vein wall another not considering vein wall. Again temperature was little lower at blood vessel side when vein wall was not considered, But this trend changed when vein wall was considered, In this case temperature was higher at blood vessel side.

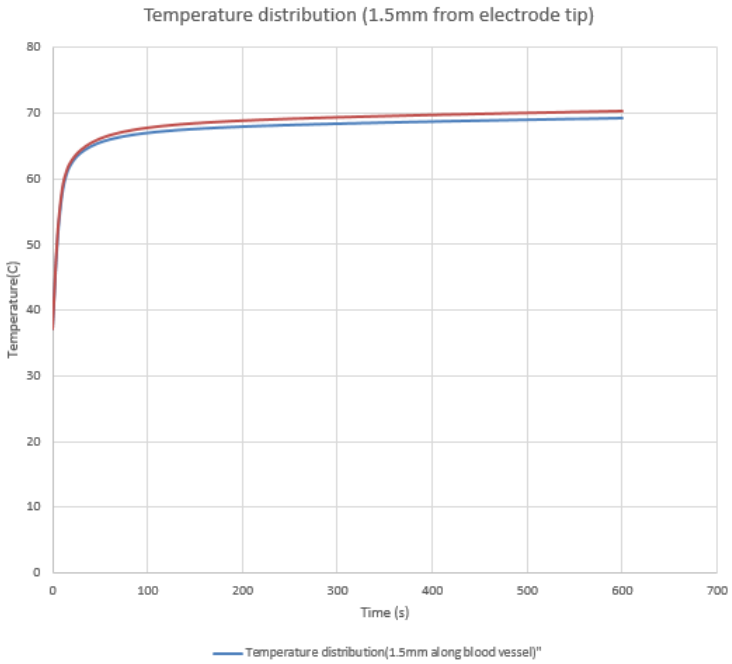

Figure 23 shows variation of temperature between equally spaced (1.5mm) one in blood vessel side and another on the opposite side(not considering vein wall).

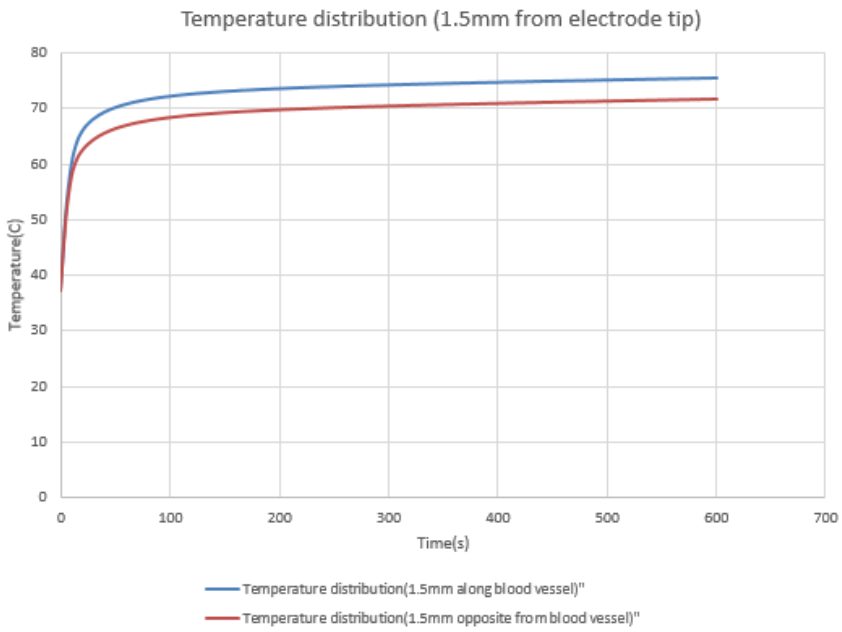

Figure 24 shows variation of temperature between equally spaced (1.5mm) one in blood vessel side and another on the opposite side (considering vein wall).

This trend continues for temperature distribution at 1.5mm distance. Again temperature was higher at blood vessel side when vein wall was considered and lower vein was not considered.

Now we decreased distance of blood vessel and electrode tip to 4mm.

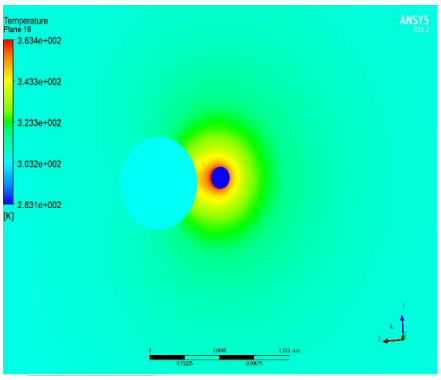

Figure 25 shows the impact of large blood vessel considering vein wall (4 mm from electrode)

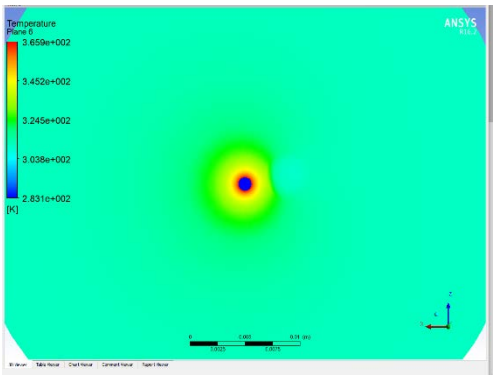

Figure 26 shows the impact of large blood vessel not considering vein wall (4 mm from electrode)

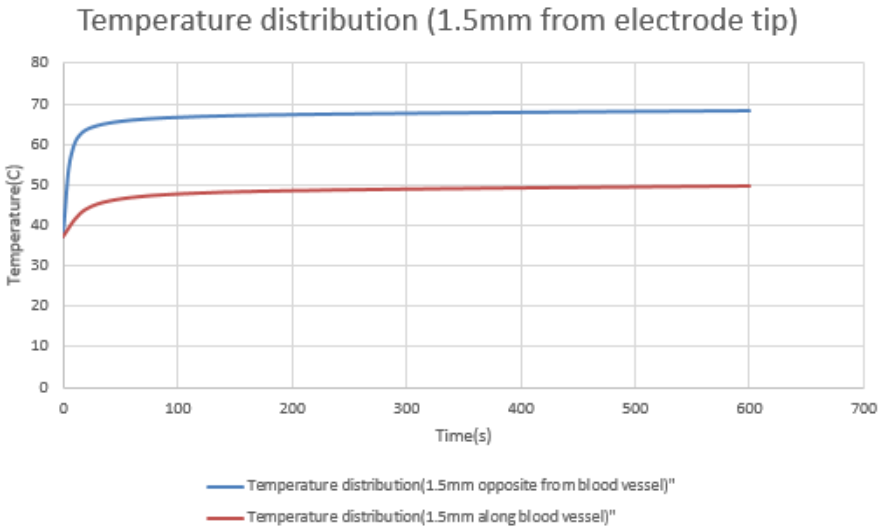

Figure 27 shows variation of temperature between equally spaced (1.5mm) one in blood vessel side and another on the opposite side (not considering vein wall).

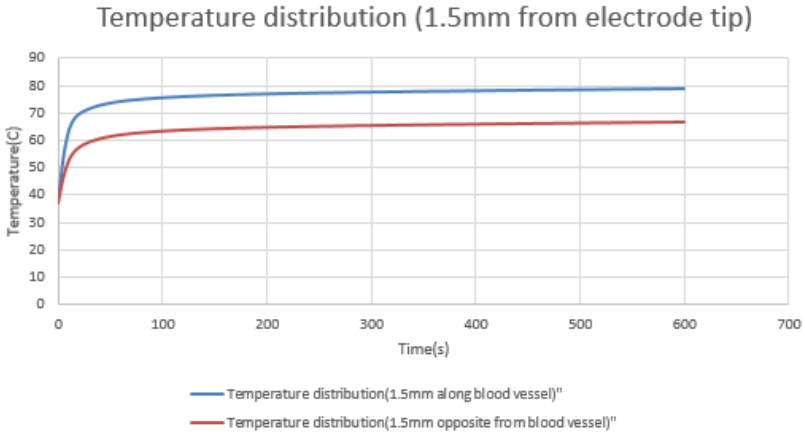

Figure 28 shows variation of temperature between equally spaced (1.5mm) one in blood vessel side and another on the opposite side (considering vein wall).

And again the same thing happened. So it can be seen that as the distance between large vessel and electrode decreased effect of sink effect of blood increased. When vein wall was not considered temperature of vessel side was less than opposite side and when vein wall was considered this trend changed and temperature was higher at vessel side. Higher temperature at vessel side may cause cell damage.

7 Discussion

When considering the results of this work we have to be aware of the large uncertainties and approximations which are associated with modelling complex biological situations with bio heat transfer models. It has to be emphasized that the results of this report only work as a prediction of the used model; the results can't in any way be extrapolated to the real in vivo situation without performing any verifying in vivo experiments. In spite of this the work can be seen as guiding in a qualitative manner when

considering RF heating and heat transfer in the vicinity of large vessels. Strengthening for the developed model is the attempt to bring together a tissue perfusion model with modelling of blood flow within large vessels. A shortcoming of the developed model is the lack of temperature dependent thermal conductivity. It is very likely that thermal conductivity of tissue depends on temperature, either by changes in blood perfusion or by changes in other tissue properties. It is likely to believe that thermal conductivity increases for relatively small increases in tissue temperature due to increasing tissue perfusion. In addition it is possible to believe that thermal conductivity decreases, to a value lower than that for 37°C, for high temperatures due to coagulation of blood in the microvascular blood flow. This behavior makes it difficult to model thermal conductivity of tissues in a reliable manner. A possible effect of temperature dependent thermal conductivity on the ablation result is a lowering of the heat sink effect for high temperatures, due to decreasing thermal conductivity. At the same time it is possible to believe that a decrease in thermal conductivity results in a heating more centralized around the electrode, resulting in a smaller ablation volume. To increase the accuracy of the second degree regression model a larger number of simulations would have been necessary; this was not possible to perform due to the limited time frame of this work.

8 Conclusions and Future Works

From the result, it has been seen that the temperature near the vein wall is more compared to the temperature at a point in the opposite direction which might cause cell damage within the vicinity of vein wall. But if we do not consider vein wall temperature distribution becomes more uniform.

Again if we increase the distance between electrode and blood vessel, the heat sink effect will decrease and that increases the simulated model's volume of ablation. For a certain distance (for our case 6mm) there was no effect of presence of blood vessel, as the distance decreased heat sink effect of blood vessel increased .If blood flow velocity and vessel diameter increases, the heat sink effect will increase and that decreases simulated model's ablation volume, And increased blood flow may help to lower temperature at vein wall help preventing cell damage.

Since experimental verification is not done, a more accurate model can be developed in the future by comparing between the practical experiments and the simulation results. We can test our model by changing number of vessel, dimensions and parameters such as blood flow velocity, distance between electrode and vessel, angle between RF electrode and blood vessel, treatment time and applied power

REFERENCES

[1] "Adult Primary Liver Cancer Treatment (PDQ®)–Patient Version". NCI. 6 July 2016. Retrieved 29 September 2016.

[2] World Cancer Report 2014. World Health Organization. 2014. pp. Chapter 5.6. ISBN 9283204298.

[3] GBD 2013 Mortality and Causes of Death, Collaborators (17 December 2014). "Global, regional, and national age-sex specific all-cause and cause-specific mortality for 240 causes of death, 1990-2013: a systematic analysis for the Global Burden of Disease Study 2013.". Lancet. 385: 117–71. doi:10.1016/S0140-6736(14)61682-2. PMC 4340604Freely accessible. PMID 25530442

[4] Tungjitkusolmun S, Tyler Staelin S, Haemmerich D, Tsai J-Z, Cao H, Webster J G, Lee F T, Mahvi D M, Vorperian V R. Three-dimensional finite-element analyses for radiofrequency hepatic tumour ablation. IEEE Trans Biomed Eng, vol. 49, No. 1, 2002.

[5] Solbiati L, Ierace T, Tonolini M, Osti V, Cova L. Radiofrequency thermal ablation of hepatic metastases. European journal of ultrasound, vol. 13 149-158, 2001.

[6] Welp C, Siebers S, Werner E, Werner J. Invetsigation of the influence of blood flow rate on large vessel cooling in hepatic radiofrequencey ablation. Biomed Tech, vol. 51 337-346, 2006.

[7] Hammerich D, Wright A W, Mahvi D M, Lee Jr F T, Webster J G. Hepatic bipolar radiofrequency ablation creates coagulation zones close to blood vessels: a finite element study. Medical & biological engineering & computing, vol. 41, 317-323, 2003.

[8] Kolios M C, Sherar M D Hunt J W. Large blood vessel cooling in heated tissues: a numerical study. Phys. Med. Biol., vol. 40 477-494, 1995.

[9] Gilliams A R, Liver ablation therapy, a review article. The British journal of radiology, vol. 77 713-723, 2004.

[10] Valleylab Cool-tipTM RF ablation system, product information. Available at: http://www.cool-tiprf.com/pdf/cool-tip_ss.pdf, accessed: 2007-12-20.

[11] http://www.cool-tiprf.com/index.html surfed on May 2010

[12] Dos Santo I, Haemmerich D, da Silva Pinheiro C, Ferreira da Rocha A, Effect of variable heat transfer coefficient on tissue temperature next to a large vessel during radiofrequency tumor ablation, BioMedical Engineering OnLine, 7 -21, 2008.

[13] Wren J, On medical thermal treatment –modelling, simulationand experiments, Dissertations no. 763, Linköpings University, 2002.

[14] Duck F, Physical properties of tissue, Academic press, London, U.K, 1990.

[15] Berjano E J. Theoretical modelling for radiofrequency ablation: state-of-the-art and challenges for the future. Biomedical engineering online, vol. 5:24, 2006.

[16] Wren J, On medical thermal treatment –modelling, simulationand experiments, Dissertations no. 763, Linköpings University, 2002.

[17] Haemmerich D, Laeseke P F. Thermal tumour abalation: devices, clinical applications and future directions. International journal of hyperthermia, vol. 21:8 755-760, 2005.

[18] Latif M J, Heat Convection, Springer, Heidelberg, Germany, 2006.

[19] http://www.cvphysiology.com/Hemodynamics/H006.htm surfed on November 2010

[20] Miguel A. F., de O Nascimento F. A, da Rocha A. F, dos Santos I, An instrument to measure the convective heat transfer coefficient on large vessels. Conf. Proc. IEEE Eng Med Biol. Soc, 2008.

[21] P. Keangin, et al., An analysis of heat transfer in liver tissue during microwave ablation using single and double slot antenna, Int. Commun. Heat Mass Transf. (2011), doi:10.1016/j.icheatmasstransfer.2011.03.027

[22] Material property values used in the study obtained from Mordon et al. (2006) and Agalar et al. (2012) .

[23] Berjano EJ. Theoretical modeling for radiofrequencyablation: stateofthe-art and Challenges for the future. Biomed Eng Online. 2006. Apr 18;5:24.

[24] Ottosen N, Petersson H, Introduction to the finite element method, Prentice Hallinternational, UK, 1992.

[25] Montree Chaichanyut and Supan Tungjitkusolmun, Microwave Ablation Using Four-Tine Antenna: Effects of Blood Flow Velocity, Vessel Location, and Total Displacement on Porous Hepatic Cancer Tissue,2016.

